FARMER LABS / PLANETARY DEFENCE

ARGUS-PD/POD-7K Paper I

Parametric Design-Space Analysis of a Modular Projectile Family and Electromagnetic Launch Interface

Christopher I. V. Farmer

Series Paper I • Independent preprint for technical review

JULY 2026

complete moving mass • projectile family • 150 GJ frontier • launch interface

Abstract

This paper examines the projectile-side design space of a hypothetical seven-kilometre electromagnetic planetary-defence research system. Its contribution is methodological rather than demonstrative: it couples moving mass, release speed, kinetic energy, momentum, acceleration length, ideal force-density screening, energy-storage demand, launch-interface mass and arrival-time constraints in one reproducible model. The reference point is a **0.300 kg complete moving assembly** released at 1.000×10^{6} m s^{-1}. That definition resolves a material contradiction in earlier drafts, which simultaneously assigned 0.300 kg to a solid projectile core and treated a large collar and release package as additional uncounted mass.

The corrected 0.300 kg study allocation assigns 0.150 kg to the structural core, 0.015 kg to a functional skin, 0.020 kg to a load spreader, 0.090 kg to an illustrative 0.200 m^2 coupling collar, and 0.025 kg to guidance, release and other moving hardware. This closes arithmetically but not experimentally: the implied collar areal density of 0.45 kg m^{-2}, its load transfer, its field coupling and its separation remain test gates.

At the reference point the assembly carries 150 GJ and 300 kN s. Constant acceleration over 7,000 m requires 14 ms, 21.429 MN mean force and 10.714 TW mean mechanical power. At an explicitly assumed 35% electrical-to-moving-mass efficiency and 20% installed reserve, admitted energy is 428.571 GJ and installed nameplate is 514.286 GJ. Spreading mean force over 0.200 m^2 corresponds to an ideal Maxwell-pressure field of 16.410 T; applying it through the 50 mm core footprint would correspond to about 166 T. Maxwell pressure is used only as a force-density ceiling. It is not treated as an accelerator topology or evidence of manufacturability.

A multi-objective grid subject to a 150 GJ mechanical ceiling produces a non-dominated frontier between speed and direct momentum. The familiar 0.300 kg/1,000 km s^{-1}, 3.333 kg/300 km s^{-1}, 13.333 kg/150 km s^{-1}, and 30 kg/100 km s^{-1} points are therefore mission cases on a continuous frontier, not proof of a single optimum. Selection is circumstance-based: among members that can reach a declared intercept point within the warning window, the slowest member supplies the greatest direct impulse at the common energy ceiling. A companion generic scenario screen shows that even the 30 kg member is not a defensible single-shot solution for a 140 m or larger target at 0.1-5 AU. Material evidence supports diamond and boron-doped diamond as candidate thermal and electronic constituents, but not as a magic monolithic structure. High boron concentration can reduce elastic constants, hardness and thermal conductivity, so doping level, defect population and temperature-dependent properties must be specified rather than inherited from pure diamond. Interplanetary dust and residual gas are first-order flight constraints: published hypervelocity studies support local crater, vapour and impact-plasma

formation, but not survival of a macroscopic solid at 100-1,000 km s^{-1}. An Earth-atmosphere trajectory is treated as ablation, ionisation, fragmentation and distributed energy deposition, not intact arrival. The preferred research article is a segmented, inspected core with a thin functional surface and a mechanically distinct collar. The paper concludes that the conservation and trade-space model is reproducible; the coupling topology, moving-mass closure, pulse store, release dynamics and impact coupling are not validated engineering.

Keywords: planetary defence; electromagnetic acceleration; design-space analysis; Pareto frontier; boron-doped diamond; pulse power; moving-mass closure; uncertainty.

1. Research question and evidentiary boundary

The research question is:

> *Given a fixed 7,000 m active length and a civil, space-only planetary-defence purpose, what combinations of complete moving mass, release speed, coupling area and material architecture survive conservation constraints, and which observations or tests would falsify them?*

The word *feasible* is divided into four levels throughout this series.

1. **Conservation-law consistent:** the stated mass, energy, momentum and force relations are mutually consistent.
2. **Parametrically expressible:** a finite set of dimensions and component duties can be stated without internal contradiction.
3. **Engineering demonstrated:** representative integrated hardware has met the relevant loads, efficiency, life and fault requirements.
4. **Mission demonstrated:** target-specific dynamics, impact response, navigation covariance, safety and lawful authorisation support a defined civil mission.

This paper establishes results only at the first level and portions of the second. No published apparatus has accelerated an intact 0.300 kg assembly to 1,000 km s^{-1}, transferred 150 GJ to it in 14 ms, or demonstrated a reusable half-metre-class moving interface at the stated field and acceleration. Microscopic particles and laser-driven plasma have reached much higher speeds than macroscopic electromagnetic launchers, but scale is the unresolved variable, not a footnote [1-4].

The paper deliberately excludes operational trajectories, target solutions, firing logic and command architecture. Flight time is reported only as the screening quotient R/v, not as an intercept solution.

2. Controlled definitions and corrected system boundary

2.1 Complete moving mass

The controlling mass is

$$m_{total} = m_{core} + m_{skin} + m_{load} + m_{collar} + m_{guidance} + m_{release} + m_{other}. \tag{1}$$

Every term that is accelerated through the full 7 km contributes to kinetic energy, force, pulse demand and launcher reaction. A component may be excluded only if it is demonstrably stationary or joins after acceleration. This rule withdraws all earlier readings in which a 0.300 kg core was combined with an unaccounted collar.

The reference allocation is a controlled hypothesis:

Moving component	Study allocation (kg)	Status
Structural core	0.150	allocation; material not selected
Functional skin	0.015	allocation; thickness and doping open
Load spreader	0.020	allocation; interface open
Coupling collar	0.090	allocation; 0.45 kg m^{-2} at 0.200 m^2
Guidance and telemetry	0.010	allocation; survivability open
Release interface	0.010	allocation; separation open
Other moving hardware	0.005	explicit contingency
Complete moving assembly	**0.300**	controlling mass

This table is a ledger, not a bill of materials. It is intentionally demanding. If the collar, release mechanism or guidance package cannot fit within the allocation, m_{total} rises and every dependent quantity must be recomputed.

2.2 Geometry implied by the correction

For a regular 32-gon with vertex diameter $D = 0.050$ m and $n = 32$,

$$A_{32} = \frac{n}{2}\left(\frac{D}{2}\right)^2 \sin\left(\frac{2\pi}{n}\right) = 1.9509 \times 10^{-3} m^2. \tag{2}$$

At diamond density $3,510$ kg m^{-3}, a **0.150 kg** uniform diamond-equivalent core would be about 21.9 mm long. The earlier 43.8 mm figure corresponded to assigning the entire 0.300 kg to the core and is withdrawn. Real segmented or composite geometry will differ. For heavier family members, core length is not reported until an explicit member-specific mass breakdown is provided.

2.3 The collar is a hypothesis, not invisible mass

The reference collar has 0.200 m^2 active area, equivalent to a circular diameter of 0.505 m. A 0.090 kg allocation implies an areal density of 0.45 kg m^{-2}. Drawing that areal density as a thin membrane, mesh or composite field structure is not the difficulty. The difficulty is everything the collar must do at the same time:

- maintaining the active electromagnetic area while transferring about 21.4 MN mean axial force;
- holding centre of magnetic force sufficiently close to centre of mass;
- limiting eddy-current and dielectric loss during a millisecond pulse train;
- surviving the acceleration environment and separating without a hazardous fragment field; and
- demonstrating that conductor, insulation, substrate, instrumentation and release hardware all fit inside the mass allocation.

Failure of any one condition increases moving mass or reduces the permitted operating point. The collar is therefore the first coupled experimental gate.

3. Governing parametric model

3.1 Energy, momentum, acceleration and time

For complete moving mass m, release speed v, and active length L,

$$E_k = \frac{1}{2} m v^2, p = m v, \tag{3}$$

$$a = \frac{v^2}{2L}, t_L = \frac{2L}{v}, \acute{F} = \frac{E_k}{L}. \tag{4}$$

Under the constant-force screen,

$$\acute{P}_{mech} = \frac{E_k}{t_L}, P_{exit,mech} = \acute{F} v = 2 \acute{P}_{mech}. \tag{5}$$

With admitted efficiency η_e and installed reserve r,

$$E_{admit} = \frac{E_k}{\eta_e}, E_{nameplate} = (1+r) E_{admit}. \tag{6}$$

The adopted values $\eta_e = 0.35$ and $r = 0.20$ are study assumptions. They are not measured efficiencies or reliability margins. A lower measured efficiency increases storage, waste heat and radiator duty as $1/\eta_e$.

3.2 Reference calculation

For $m = 0.300$ kg, $v = 1.000 \times 10^6$ m s^{-1}, and $L = 7{,}000$ m:

Quantity	Recomputed value
Kinetic energy	150.000 GJ
Momentum	300.000 kN s
Mean acceleration	7.143×10^7 m s^{-2}
Launcher transit	14.000 ms
Mean axial force	21.429 MN
Mean mechanical power	10.714 TW
Exit mechanical power	21.429 TW
Admitted energy at 35%	428.571 GJ
Installed nameplate with 20% reserve	514.286 GJ
Mean admitted power	30.612 TW
Exit admitted power	61.224 TW

These are conservation results. They do not establish a waveform, conductor, switch, stress path or storage technology.

3.3 Ideal force-density screen

The ideal excluded-field magnetic pressure is

$$p_B = \frac{B^2}{2\mu_0}. \tag{7}$$

If the entire mean axial force were distributed uniformly over active area A_c,

$$B_{ideal} = \sqrt{\frac{2\mu_0 \acute{F}}{A_c}}, A_{c,min} = \frac{2\mu_0 \acute{F}}{B_{max}^2}. \quad (8)$$

At 21.429 MN and 0.200 m², Eq. (8) gives 16.410 T. Over the 50 mm core area it gives about 166 T. This contrast justifies separating a narrow structural core from a wide coupling interface.

Equation (8) is an **ideal upper-bound screen**. It assumes uniform pressure and omits fringe fields, leakage, armature current distribution, field penetration, dynamic stability, structural concentration and losses. It cannot be cited as evidence that a launcher exists.

3.4 Energy accounting is not hardware

Dividing 514.286 GJ into 6,000 equal accounting tranches gives 85.714 MJ per tranche. A tranche has no implicit voltage, capacitance, mass, inductance, chemistry or discharge curve. It is useful for fault and energy bookkeeping only.

Current stationary products illustrate the separation between bulk energy and pulse power. A four-hour Tesla Megapack configuration contains about 3,916 kWh and is limited to about 979 kW; its energy is relevant to slow buffering but not to a tens-of-terawatts discharge [5]. The General Atomics 3283CMX2640 pulse capacitor stores 255 kJ at about 140 kg, so direct substitution would require more than two million units before switches, buswork, containment or space qualification [6]. These comparisons do not nominate products. They show why the storage problem must be modelled in energy, specific energy, pulse power, current, voltage, inductance, life and thermal terms simultaneously.

4. Electromagnetic interface topologies

The system requires an electromagnetic topology rather than a static-field analogy. Two candidate classes are retained for research comparison.

4.1 Switched-inductance travelling cell

A conductive or superconducting collar can couple to sequential external coils through position-dependent mutual inductance. A circuit-level force term has the form

$$F_x \simeq I_s I_a \frac{dM}{dx} + \frac{1}{2} I_a^2 \frac{dL_a}{dx}, \quad (9)$$

where I_s is a stator current, I_a an armature or collar current, M mutual inductance and L_a an effective armature inductance. This topology must close current induction or injection, phase timing, parasitic inductance, field penetration, skin and proximity loss, switching overvoltage, axial stability and energy recovery. Ferromagnetic-reluctance interpretations are not assumed at the 16 T scale because saturation would dominate ordinary magnetic materials.

4.2 Linear-synchronous superconducting interface

A second class uses a persistent or actively driven collar field coupled to a travelling external field. The same mutual-inductance gradient governs force, but the collar current and quench margin become explicit design variables. Static trapped-field results in REBCO stacks demonstrate relevant field magnitude under specialised cryogenic conditions [7]. They do not demonstrate a metre-class aperture, rapid field reversal, multi-million-g structural survival, dynamic force transfer or repetitive operation.

4.3 Selection criteria

The topology down-selection shall be based on a measured cell model containing:

- current and voltage waveforms;
- $M(x)$, dM/dx, self-inductance and parasitic inductance;
- field distribution and transverse stability;
- conductor critical surface and quench margin;
- collar eddy-current, hysteretic and dielectric loss;
- switching error and fault energy;
- recoverable energy fraction;
- force transmitted into the support structure; and
- life under representative pulse and thermal cycles.

Until those quantities exist, the 16.410 T result remains a screen, not a design.

5. Material and assembly architecture

5.1 What diamond evidence supports

Diamond offers exceptional thermal conductivity, stiffness and high-pressure strength, and shock experiments show residual strength under extreme compression [8,9]. Heavy boron doping can produce metallic transport and superconductivity [10-12]. These facts justify coupon research. They do not show that a uniformly doped diamond monolith preserves undoped strength; in fact, experimental and computational work reports mechanical softening with boron concentration [13].

The term *boron-doped diamond projectile* is therefore narrowed to a functional architecture:

- a structural core or segmented load path selected for flaw tolerance and impact purpose;
- a thin, spatially graded BDD surface where electronic function is required;
- a load spreader that avoids point loading the core;
- an electromagnetically active collar; and
- a release interface whose fragments and residual state are controlled.

5.2 The role of 32 faces

Thirty-two faces are treated as an interface standard, not a new material state. Nothing in this paper justifies the number. Faceting could supply repeatable inspection datums, sector boundaries for conductive patterns, load-transfer flats and clocking references, but none of those functions selects 32 over any other count. The geometry must be compared against circular, lower-facet and segmented alternatives. The number 32 is retained only if tests show an advantage in field uniformity, assembly, metrology or fracture control.

5.3 Material candidates

Candidate	Useful evidence	Principal reservation	Present study role
CVD/PCD diamond	thermal transport, stiffness and 5-6 MPa m□$^{1/2}$ measured toughness [31]	brittle flaw sensitivity; microstructure-dependent properties; scale [32]	structural coupon and thermal spreader
Boron-doped diamond	controllable electronic function [10-13,25]	no universal property set; heavy doping can soften response	thin or graded functional layer
Diamond-SiC composite	10.4 ± 4.0 GPa microscale interface strength in one infiltrated material [33]	residual silicon, interface scatter and no whole-article rate validation	scalable hybrid-core candidate
Toughened silicon carbide	ABC-SiC laboratory toughness 6.2-7.2 MPa m□$^{1/2}$ at room temperature [34]	processing-sensitive grain boundaries; brittle dynamic failure	structural ceramic comparator
Boron carbide	low density, hardness and thermal stability	impact-induced local amorphisation and crack initiation [35]	low-mass hard-ceramic comparator
Tungsten or tungsten alloy	density, compactness and measured fracture response	moving-mass penalty; room-temperature brittleness depends	metal core, collar or sacrificial-nose comparator

Candidate	Useful evidence	Principal reservation	Present study role
		on microstructure [36]	
Carbon-carbon or graphite-rich layer	low atomic number; ultrafast-probe erosion studies [38]	anisotropy, porosity, joining and no ARGUS ballistic limit	sacrificial nose or erosion layer
Graded hybrid	separates structural, electrical and shielding functions	interface qualification and residual stress dominate	architecture hypothesis

No material ranking can be independent of the target response, the moving-mass budget and the interface topology. At fixed m and v, changing material does not change energy or momentum; it changes geometry, load path, manufacturability, failure mode and coupling.

5.4 Boron concentration and acceleration state

Boron-doped diamond is not one material. Liu et al. found low-concentration single-crystal BDD close to natural diamond in elastic response, but reported reductions of about 2.4%-3.3% in elastic constants and a much larger hardness reduction at 2,000-3,000 ppm boron [13]. Prikhodko et al. measured thermal conductivity about tenfold below high-quality type-IIa diamond near 100 K for a BDD sample containing approximately 10^{19} cm^{-3} boron, with a difference below 30% above room temperature [25]. These are material-specific measurements, not universal correction factors.

The projectile specification shall therefore declare doping concentration, uniformity, crystal form and orientation, grain or flaw population, temperature-dependent conductivity, resistivity, tensile and fracture allowables, and residual stress. A thin functional BDD layer may be preferable to a uniformly doped structural core if electrical function can be separated from the load path.

Bulk velocity does not itself heat the co-moving article. The threatening state variables are acceleration stress, electromagnetic and interface heating, stress waves, charge, and collisions after release. For the 21.9 mm diamond-equivalent reference core, a one-dimensional end-loaded scale $\rho a L_c$ is about 5.49 GPa at 1,000 km s^{-1} over 7 km. Distributed collar loading may reduce that value, while asymmetry, reflections and flaws can worsen local tension. It is a transient-fracture test requirement, not a strength margin.

5.5 Lower-bound dust-fracture screen

The material comparison can support a mathematical screening threshold, but not a validated breakup diameter. For a linear-elastic brittle surrogate,

$$E' = \frac{E}{1-\nu^2}, G_{Ic} = \frac{K_{Ic}^2}{E'}, E_{section} = G_{Ic} A_p. \quad (9a)$$

Using $K_{Ic} = 5.6$ MPa m□$^{1/2}$ from CVD-diamond tests [31], $E = 830$ GPa and $\nu = 0.10$ as an illustrative microcrystalline-diamond surrogate consistent with the scale in [32], gives $G_{Ic} = 37.4$ J m^{-2} and 0.0734 J for one ideal crack across a 50 mm circular section. If collision-energy coupling into that crack mode is η_c, the energy-equivalent grain is

$$m_{d,*} = \frac{2 E_{section}}{\eta_c v_r^2}, d_{d,*} = \left(\frac{6 m_{d,*}}{\pi \rho_d} \right)^{1/3}. \tag{9b}$$

At $\rho_d = 2,500$ kg m^{-3}, the 100%/1% coupling screens are 22.4/104 µm at 100 km s^{-1}, 10.4/48.2 µm at 316 km s^{-1} and 4.82/22.4 µm at 1,000 km s^{-1}. The full table is machine-readable in dust_fracture_energy_screen.csv.

These are deliberately conservative **surface-creation-energy** thresholds. They omit crater confinement, impact location, attenuation, crack initiation and branching, stress-wave superposition, fragment motion, phase change, dynamic toughening, the flaw distribution and the difference between undoped CVD diamond and a specified BDD or composite architecture. The values are therefore triggers for matched-material impact tests and dynamic-fracture hydrocodes, not ballistic limits or predictions of breakup.

6. Reproducible design-space analysis

6.1 Decision variables, constraints and objectives

The accompanying code evaluates:

$$0.300 \le m \le 30\,kg, 100 \le v \le 1,000\,km\,s^{-1}, \tag{10}$$

subject to

$$E_k \le 150\,GJ, L = 7,000\,m, B_{ideal} \le 16.5\,T \tag{11}$$

with coupling area allowed to grow as required by Eq. (8). The performance objectives are to maximise speed and direct momentum. Installed energy, required area, screen flight time and covariance-derived miss scale remain reported attributes. This creates an explicit Pareto problem: no point is preferred if another point does not improve one objective without worsening the other.

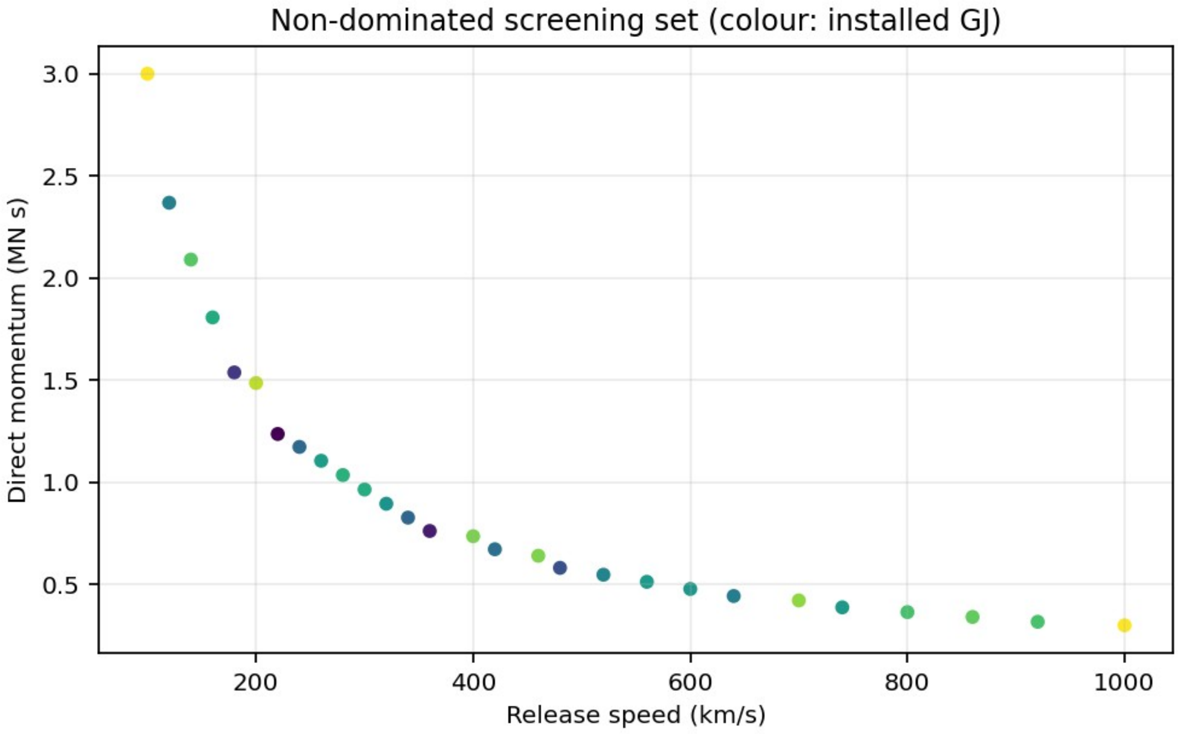

Non-dominated speed-momentum screening set. Colour denotes installed nameplate energy under the adopted efficiency and reserve assumptions. This is a parametric screen, not a mission trajectory.

6.2 The 150 GJ reference family

For a fixed energy E,

$$m = \frac{2E}{v^2}, p = \frac{2E}{v}. \tag{12}$$

Speed therefore buys shorter ideal flight time while reducing direct momentum at fixed energy.

Case	Complete moving mass	Speed	Momentum	$0.5\,AU/v$
R-DART screen	0.300 kg	1,000 km s^{-1}	0.300 MN s	0.866 d
Q-DART screen	1.200 kg	500 km s^{-1}	0.600 MN s	1.731 d
V-DART screen	3.333 kg	300 km s^{-1}	1.000 MN s	2.886 d
M-DART screen	13.333 kg	150 km s^{-1}	2.000 MN s	5.772 d
T-DART screen	30.000 kg	100 km s^{-1}	3.000 MN s	8.657 d

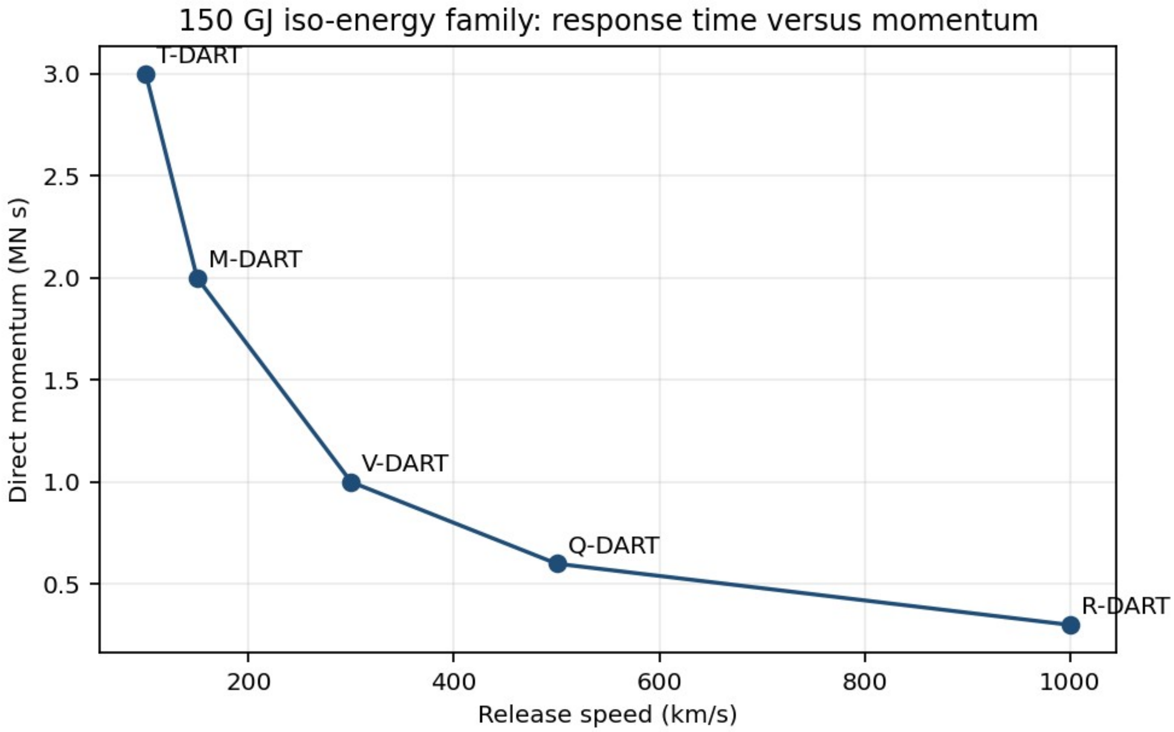

The 150 GJ family. Slower members have more direct momentum; faster members have shorter ideal line-of-flight time.

The labels are research shorthand. They are not approved articles, mission recommendations or safety findings. In particular, a heavier member requires its own mass budget, release package and environmental analysis.

6.3 Why this is optimisation rather than a trade-study label

The model stores every admissible grid point, performs an exact non-dominance test and exports the frontier. Mission selection then requires an explicit preference or constraint:

- a response-time case selects the highest speed that satisfies energy, coupling, covariance and survival constraints;
- a coherent-impulse case selects the greatest momentum that still arrives within the available warning window; and
- a balanced case imposes minimum speed and momentum thresholds, then minimises installed energy or test burden.

No scalar weighting is hidden. If a future study applies weights, their values and sensitivity must be published.

6.4 Circumstance-based selection

The frontier becomes a decision only after experimental objective, warning and target circumstances are declared. A companion launcher science and application-envelope study applies both scientific-use and generic inbound screens to the family [23]. Its mission-selection rule is simple: reject every member that cannot reach the declared intercept distance inside the warning window, then choose the slowest remaining member when coherent direct impulse is the objective. At the common 150 GJ ceiling, this maximises momentum and reduces module power, but increases moving mass, recoil and flight time.

That screen also prevents “most effective” from becoming an unsupported universal claim. With an illustrative 20 km s^{-1} inbound target, rocky density of 2,600 kg m^{-3} and $\beta = 3$, T-DART is the strongest admissible family member when time permits. It still does not produce a single-shot Earth-radius-class displacement for a 140 m or larger target at generic intercept distances of 0.1-5 AU. Target size and warning therefore determine whether the family describes a small-body multi-shot research case or an energy scale too small for the threat.

7. Navigation and uncertainty as constraints

A point estimate of accuracy is inadequate. A minimal one-sigma screen is

$$\sigma_{miss}^2 = (R\sigma_\theta)^2 + (v\sigma_t)^2 + \sigma_{target}^2 + \sigma_{model}^2, \quad (13)$$

where σ_θ is angular release uncertainty, σ_t timing uncertainty, and the remaining terms represent target-state and model covariance. Equation (13) is not a guidance design. It shows the coupling: angular error scales with range and timing error scales with speed. Higher speed shortens exposure to target evolution but increases along-track distance per unit timing error and transverse correction cost per unit angle.

DART demonstrated autonomous optical terminal navigation and measurable asteroid-orbit change [14-17]. It did not demonstrate the present velocity, mass, pulse or correction regime. Any statement of mission feasibility requires a full covariance propagated through a target-specific transfer and impact model.

8. Impact response and environmental boundary

For an asteroid of mass M_a, the direct impulse screen is

$$\Delta v_a = \frac{\beta m v_{rel}}{M_a}, \tag{14}$$

where β represents ejecta momentum enhancement. DART showed that β can exceed unity for a particular target and geometry [16]. It is not a universal constant. Porosity, cohesion, shape, obliquity and impact speed change both momentum transfer and disruption risk [18-22].

At extreme velocity, extrapolation beyond validated hydrocodes and experiments is substantial. Delivered kinetic energy is calculable; useful deflection is not. The impact programme must therefore bracket:

- coherent momentum transfer;
- cratering and ejecta enhancement;
- fragmentation and fragment-dispersion risk;
- ionisation and vaporisation;
- material-dependent coupling; and
- uncertainty in target structure.

Space is not a complete vacuum. NASA's Meteoroid Engineering Model resolves meteoroid flux by mass, speed, density and direction, and a trajectory-specific run is required before projectile survival can be claimed [24]. NASA and peer-reviewed hypervelocity studies describe vaporisation, ionisation, cratering and impact-plasma formation [26,27]. At 1,000 km s^{-1}, a 1 μg grain carries 500 J in the projectile frame. That energy is deposited locally; it does not automatically release the full projectile energy. Catastrophic breakup depends on impact position, grain size, material flaws, stress-wave propagation and accumulated fluence.

Two research analogues define a stronger method. The Solar Probe Plus/Parker Solar Probe shield study developed a test-anchored shock-hydrocode ballistic-limit equation over 7-150 km s^{-1} for a declared Kapton-standoff-Ti configuration [37]. Its hundreds-of-micrometres critical grains cannot be transferred to this projectile, but its material-specific workflow can. Hoang et al. modelled cratering, melting and cumulative erosion of a relativistic wafer by interstellar dust and gas [38]. Its environment, speed and geometry are also different; it is evidence for treating both rare large impacts and accumulated small-particle damage, not evidence for an ARGUS survival margin.

For an already-defined critical population with uniform number density $n_{\geq m_*}$, projected area A_p and path D,

$$\lambda = A_p n_{\geq m_*} D, P(N \geq k) = 1 - e^{-\lambda} \sum_{j=0}^{k-1} \frac{\lambda^j}{j!}. \tag{14a}$$

For a 50 mm projected diameter, the fluences required for 1%, 10%, 50% and 90% probability of at least one critical hit are 5.12, 53.7, 353 and 1,173 m^{-2}. The equivalent uniform number densities for 50% probability are 3.53×10^{-4}, 3.53×10^{-7} and 2.36×10^{-9} m^{-3} over 1,000 km, 1,000,000 km and 1 au respectively. These are sensitivity thresholds, not estimates of the actual space environment. MEM3 or an equivalent measured directional distribution must supply the population, transformed into the unusually fast projectile frame.

“Enough smaller things” requires a compound damage model rather than a chosen integer alone:

$$D=\sum_i \psi\left(m_i, v_{r,i}, x_i, \theta_i; M, F\right), P_{fail}=P\left(D\geq 1\right), \tag{14b}$$

where M is material state and F its flaw population. The calibrated increment ψ must capture crater overlap, nose recession, charge, angular impulse, stress-wave interaction and crack coalescence.

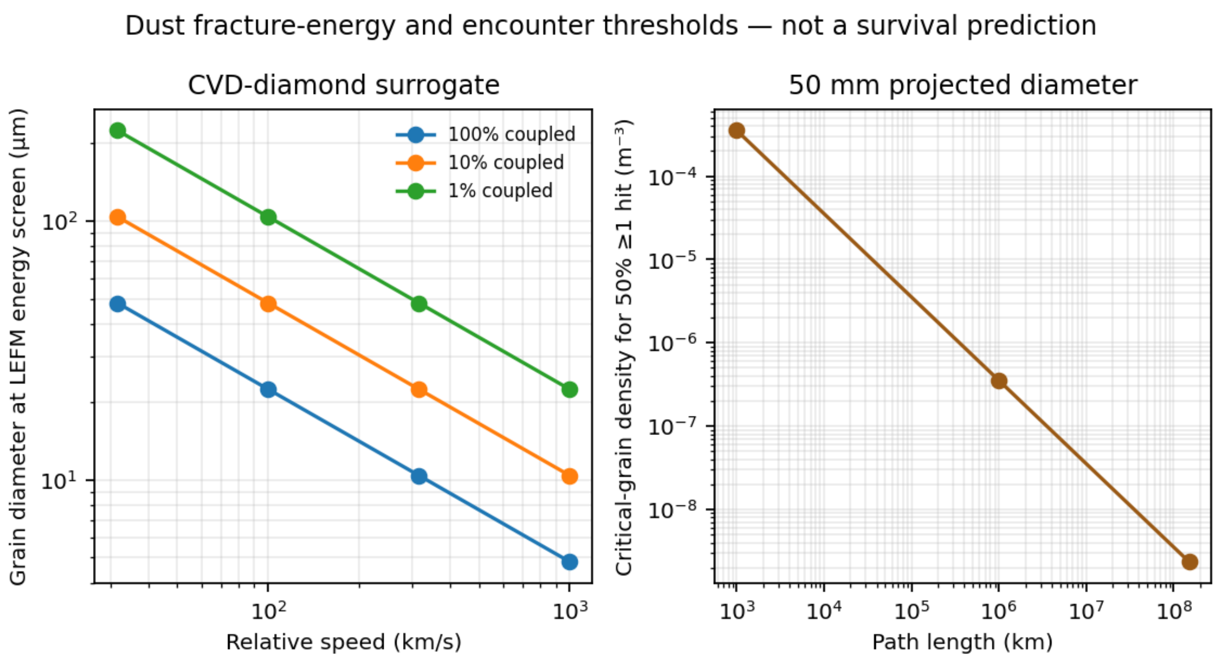

CVD-diamond surrogate fracture-energy and Poisson encounter thresholds. The figure is a parametric screen, not a survival prediction.

The nearest macroscopic solid-projectile experiment identified by this audit demonstrated an 8 mm, 0.36 g magnesium article at 10.4 km s^{-1} [28]. A microgram-scale plasma has been accelerated to about 140 km s^{-1} [4], but this does not validate an intact macroscopic solid. The 100-1,000 km s^{-1} family is therefore outside the experimental solid-projectile envelope.

Earth-atmosphere passage is not an intact-arrival mode. The atmospheric column is approximately 1.03×10^{4} kg m^{-2}; a 50 mm circular cross-section geometrically intercepts about 20.3 kg, roughly 68 times the complete 0.300 kg reference moving mass. Coupled ablation and radiation models are required even for much slower sample-return entries [29], and meteor research shows sputtering and ablation at much lower speeds [30]. At the proposed speeds the energy would be distributed into shock-heated gas, plasma, radiation, vapour, fragments and acoustic motion. Breakup and intense light/plasma are expected, but exact altitude and optical yield require nonequilibrium radiation-hydrodynamics rather than assertion.

All Earth-intersecting states are excluded from the intended research envelope. The flight-survival evidence gate is a coupled dust-flux, residual-gas, charge, ablation and stochastic-fracture model validated against representative impacts.

9. Falsification and development gates

Gate	Test article	Required evidence	Stop or redesign condition
P1	matched material set: diamond, BDD, diamond-SiC, SiC, B4C, W and carbon-rich layer	measured strength, conductivity, fracture and failure statistics	no qualified load path or functional layer
P2	collar coupon and load spreader	field coupling, areal mass and force transfer	mass budget or stress cannot close
P3	representative electromagnetic cell	measured $M(x)$, force, efficiency, stability and loss	topology cannot approach the declared duty with margin
P4	pulse-store module	energy, power, inductance, life and fault containment	extrapolated installation is incompatible with deployment
P5	accelerated subscale assembly	centring, telemetry and release covariance	uncontrolled separation or structural failure
P6	dust/gas exposure article	material-specific crater, plasma, charge and dynamic-fracture thresholds	no credible flight-survival envelope
P7	trajectory environment model	particle-frame fluence, Poisson critical-hit and compound cumulative-damage probability	survival requirement not met
P8	impact campaign	validated response across target classes	no defensible effect envelope

The 1,000 km s^{-1} point is reduced or withdrawn if a lower-level gate shows no scalable path. Passing a coupon gate does not validate the next level.

10. Results, limitations and conclusion

The reproducible results are:

1. the reference conservation arithmetic is correct when 0.300 kg means the complete moving assembly;
2. the earlier full-core geometry is not correct under that definition and is withdrawn;
3. a 0.200 m^2 active interface produces a 16.410 T ideal Maxwell-pressure screen at 150 GJ over 7 km, but this is not a topology;
4. the collar allocation is itself an aggressive, testable hypothesis;
5. the speed-momentum trade under an energy ceiling is a Pareto frontier, not a unique optimum;
6. no material is selected: CVD diamond, BDD, diamond-SiC, toughened SiC, boron carbide, tungsten and carbon-rich layers have different functions and failure modes that require matched high-rate tests;
7. dust, residual gas and atmospheric passage are first-order energy-deposition and fracture constraints; the LEFM grain sizes are conservative test triggers, while trajectory fluence and compound Poisson damage govern survival probability; and
8. engineering and mission feasibility remain unestablished.

The principal limitations are the absence of a measured dynamic coupling topology, a validated moving-interface mass model, a pulse store, a representative structural experiment, a mission covariance and extreme-speed impact validation. These are not hidden behind the phrase *in principle*. They are the decisions that determine whether the research proceeds.

Declarations

Funding. No external funding is declared.

Competing interests. The author declares no competing financial interest.

Data and code availability. The complete calculation code, unit tests, machine-readable design grid, Pareto set, reference-family table, material-evidence matrix, dust-fracture and encounter-probability tables and figure scripts accompany this paper. The package contains screening calculations only. No mission-grade trajectory, targeting, electromagnetic finite-element, quench, structural or impact-hydrodynamics model is represented as available.

Dual-use boundary. The work addresses conservation, materials, qualification and governance for civil planetary defence. Terrestrial, anti-satellite, coercive and combat applications are excluded. Operational target data, firing logic and command architecture are not included.

References

1. Asay, J. R. & Hawke, R. S. *Performance Characteristics of a Three-Stage Railgun*. SAND-89-2198C (1989). https://www.osti.gov/servlets/purl/5370387.
2. Hawke, R. S. *Devices for Launching 0.1-g Projectiles to 150 km/s or More to Initiate Fusion, Part 2: Railgun Accelerators*. UCRL-52778 Part 2 (1979). https://www.osti.gov/servlets/purl/5821802.
3. Keaton, P. W. et al. A hypervelocity-microparticle-impacts laboratory with 100-km/s projectiles. *International Journal of Impact Engineering* 10, 295-308 (1990). https://doi.org/10.1016/0734-743X(90)90067-6.
4. Badziak, J. et al. Efficient acceleration of a dense plasma projectile to hyper velocities. *Laser and Particle Beams* 36, 49-54 (2018). https://doi.org/10.1017/S0263034617000945.
5. Tesla. Megapack product details: 979 kW/3,916 kWh four-hour configuration and 84,000 lb maximum weight (accessed 23 July 2026). https://www.tesla.com/megapack/design.
6. General Atomics. Series CMX self-healing energy-storage capacitors, part 3283CMX2640: 255 kJ and approximately 140 kg (accessed 23 July 2026). https://www.ga.com/capacitors/series-cmx-self-healing-energy-storage-capacitors.
7. Patel, A. et al. A trapped field of 17.7 T in a stack of high-temperature superconducting tape. *Superconductor Science and Technology* 31, 09LT01 (2018). https://doi.org/10.1088/1361-6668/aad34c.
8. MacDonald, M. J. et al. Material strength in shock-compressed diamond. *Applied Physics Letters* 116, 234104 (2020). https://doi.org/10.1063/5.0013085.
9. Swift, D. C. et al. Equation of state and strength of diamond in high-pressure ramp compression. *Physical Review B* 105, 014109 (2022). https://doi.org/10.1103/PhysRevB.105.014109.
10. Ekimov, E. A. et al. Superconductivity in diamond. *Nature* 428, 542-545 (2004). https://doi.org/10.1038/nature02449.
11. Klein, T. et al. Metal-insulator transition and superconductivity in boron-doped diamond. *Physical Review B* 75, 165313 (2007). https://doi.org/10.1103/PhysRevB.75.165313.
12. Gajewski, W. et al. Electronic and optical properties of boron-doped nanocrystalline diamond films. *Physical Review B* 79, 045206 (2009). https://doi.org/10.1103/PhysRevB.79.045206.
13. Liu, X. et al. Elastic and mechanical softening in boron-doped diamond. *Scientific Reports* 7, 42921 (2017). https://doi.org/10.1038/srep42921.
14. Adams, E. et al. *Final DART Technical Report to NASA*. NASA NTRS 20230015804 (2023). https://ntrs.nasa.gov/citations/20230015804.

15. Daly, R. T. et al. Successful kinetic impact into an asteroid for planetary defence. *Nature* 616, 443-447 (2023). https://doi.org/10.1038/s41586-023-05810-5.
16. Cheng, A. F. et al. Momentum transfer from the DART mission kinetic impact on asteroid Dimorphos. *Nature* 616, 457-460 (2023). https://doi.org/10.1038/s41586-023-05878-z.
17. Thomas, C. A. et al. Orbital-period change of Dimorphos due to the DART kinetic impact. *Nature* 616, 448-451 (2023). https://doi.org/10.1038/s41586-023-05805-2.
18. Holsapple, K. A. & Housen, K. R. Momentum transfer in asteroid impacts: theory and scaling. *Icarus* 221, 875-887 (2012). https://doi.org/10.1016/j.icarus.2012.09.022.
19. Raducan, S. D. et al. Influence of projectile geometry on momentum transfer and implications for DART. *International Journal of Impact Engineering* 162, 104147 (2022). https://doi.org/10.1016/j.ijimpeng.2021.104147.
20. Raducan, S. D., Davison, T. M. & Collins, G. S. Ejecta distribution and momentum transfer from oblique impacts. *Icarus* 374, 114793 (2022). https://doi.org/10.1016/j.icarus.2021.114793.
21. Leinhardt, Z. M. & Stewart, S. T. Collisions between gravity-dominated bodies: outcome regimes and scaling laws. *Astrophysical Journal* 745, 79 (2012). https://doi.org/10.1088/0004-637X/745/1/79.
22. Jutzi, M. & Michel, P. Hypervelocity impacts on asteroids and momentum transfer: porous-target simulations. *Icarus* 229, 247-253 (2014). https://doi.org/10.1016/j.icarus.2013.11.020.
23. Farmer, C. I. V. *ARGUS-PD/POD-7K Launcher Science and Application Envelope: Distributed Pulse-Module Architecture*, *Counter-Impulse Closure*, *Projectile-Family Physics and Space-Only Research Utility*. Version 1.0.0, companion preprint (2026).
24. Moorhead, A. V., Kingery, A. & Ehlert, S. NASA's Meteoroid Engineering Model 3 and its ability to replicate spacecraft impact rates. *Journal of Spacecraft and Rockets* 57 (2020). https://ntrs.nasa.gov/citations/20200000563.
25. Prikhodko, D. et al. Thermal conductivity of synthetic boron-doped single-crystal HPHT diamond from 20 to 400 K. *MRS Communications* 6, 71-76 (2016). https://doi.org/10.1557/mrc.2016.12.
26. Lee, N. & Close, S. Meteoroid impact detection for exploration of asteroids: small satellites for asteroid characterization. *Journal of Spacecraft and Rockets* 55 (2018). https://doi.org/10.2514/1.A33928.
27. Christoffersen, R. et al. Experimental hypervelocity dust impacts in olivine: microcraters, melt, vapour and plasma-plume evidence. *Journal of Geophysical Research: Planets* (2026). https://ntrs.nasa.gov/api/citations/20260002134/downloads/ChristoffersenEtAl-Microcraters_JGR_FinalPublished.pdf.
28. Huneault, J. et al. An explosively driven launcher capable of 10 km s^{-1} projectile velocities. *Shock Waves* 32, 569-591 (2022). https://doi.org/10.1007/s00193-022-01095-1.

29. Johnston, C. O. Study of aerothermodynamic modeling issues relevant to high-speed sample return vehicles. NATO STO-AVT-218 (2014). https://ntrs.nasa.gov/citations/20140004052.
30. Guttormsen, G., Fletcher, A. C. & Oppenheim, M. M. Atomic-scale simulations of meteor ablation. *Journal of Geophysical Research: Space Physics* 125, e2020JA028229 (2020). https://doi.org/10.1029/2020JA028229.
31. Drory, M. D., Dauskardt, R. H., Kant, A. & Ritchie, R. O. Fracture of synthetic diamond. *Journal of Applied Physics* 78, 3083-3088 (1995). https://doi.org/10.1063/1.360060.
32. Meindlhumer, M. et al. Micromechanical properties of micro- and nanocrystalline CVD diamond thin films with gradient microstructures and stresses. *Journal of Vacuum Science & Technology A* 42, 023401 (2024). https://doi.org/10.1116/6.0003235.
33. Ast, J. et al. Micro-cantilever testing of diamond-silicon carbide interfaces in silicon carbide bonded diamond materials produced by reactive silicon infiltration. *Open Ceramics* 8, 100176 (2021). https://doi.org/10.1016/j.oceram.2021.100176.
34. Chen, D., Gilbert, C. J., Zhang, X. F. & Ritchie, R. O. High-temperature cyclic fatigue-crack growth behavior in an in situ toughened silicon carbide. *Acta Materialia* 48, 659-674 (2000). https://doi.org/10.1016/S1359-6454(99)00406-1.
35. Zhang, H. et al. Impact resistance of boron carbide ceramics from hypersonic and supersonic impacts: a large-scaled molecular dynamics simulation study. *Journal of Applied Physics* 131, 135105 (2022). https://doi.org/10.1063/5.0080252.
36. Gludovatz, B., Faleschini, M., Wurster, S., Hoffmann, A. & Pippan, R. Influence of microstructure on the fracture toughness of tungsten alloys. *TMS Annual Meeting Proceedings*, 449-454 (2008). https://pure.unileoben.ac.at/ws/files/1008984/Influence_of_Microstructure_on_the_Fracture_Toughness_of_Tungsten_Alloys.pdf.
37. Iyer, K. A., Mehoke, D. S. & Batra, R. C. Interplanetary dust particle shielding capability of spacecraft multilayer insulation. *Journal of Spacecraft and Rockets* 52, 584-594 (2015). https://doi.org/10.2514/1.A33101.
38. Hoang, T., Lazarian, A., Burkhart, B. & Loeb, A. The interaction of relativistic spacecrafts with the interstellar medium. *Astrophysical Journal* 837, 5 (2017). https://doi.org/10.3847/1538-4357/aa5da6.